
FUNCTIONAL COATINGS
AND SURFACE TREATMENT

The Structure of the Surface Layer of 0.4C–1Cr Structural Steel after Finishing Stages of Machining by Cutting

M. V. Pimonov^{a, *}, D. A. Romanov^{b, c, **}, and H. Chen^{c, ***}

^a Kuzbass State Technical University, Kemerovo, 650000 Russia

^b Siberian State Industrial University, Novokuznetsk, 654006 Russia

^c Institute of Laser and Optoelectronic Intelligent Manufacturing, Wenzhou University, Zhejiang, Wenzhou, 325024 China

*e-mail: pimonovmv@kuzstu.ru

**e-mail: romanov_da@physics.sibsiu.ru

***e-mail: chenxizhang@wzu.edu.cn

Received November 22, 2019; revised March 18, 2020; accepted April 19, 2020

Abstract—The microstructure and local fields of internal stresses arising in the surface layer of 0.4C–1Cr structural alloy steel (type 40X) samples after machining by cutting are investigated. Before treatment, the samples were subjected to recrystallization annealing at a temperature of 600°C for 60 min. Sample processing was carried out in three modes: finishing (mode 1); sequential combination of roughing and semifinishing (mode 2); sequential combination of roughing, semifinishing, and finishing (mode 3). In processing modes 1, 2, and 3, chips were removed to a depth of 0.25, 1.5, and 1.75 mm, respectively. Transmission electron microscopy was used to determine the amplitude of the curvature-torsion of the crystal lattice of the phases formed, the excess dislocation density, and the amplitude of internal stresses. It was found that the main phase components in steel 40X after cutting are represented by lamellar pearlite with different morphology and fragmented and unfragmented ferrite.

Keywords: structure, machining, cutting, structural steel, phases, transmission electron microscopy

DOI: 10.1134/S2075113321030291

INTRODUCTION

Currently, parts of machinery and equipment are usually manufactured by means of sequential processing [1]. At the first stage, the product undergoes roughing [2], which is needed to give the blank the dimensions and shape close to the required ones. At the second and third stages, semifinishing [3] and finishing [4] are performed. Modern machining tools for mechanical processing allow achieving accuracy up to 0.001% [5]. The use of such an approach, when a part is cut out of a workpiece, and then allowances for semifinishing and finishing of the surface of the parts are removed, is economically inexpedient, since a significant part of the material is lost in this case [6]. Recycling of excess workpiece material is possible after its reprocessing, for example, by remelting [7].

Alternative processing methods are additive technologies [8], including construction of products layer-by-layer from molten plastic threads [9], selective laser fusion of metal powders [10], selective laser sintering of polymer powders [11], laser stereolithography, laser-assisted solidification of liquid photopolymer materials [12], multi-jet modeling using photopolymers or wax materials [13, 14], curing of liquid photopolymers by ultraviolet radiation [15], layer-by-layer

distribution of an adhesive over a gypsum powder material [16], electroexplosive additive technologies [17, 18], and others. However, in practice, after the production of parts by additive methods, their surface is usually finalized by subtractive production methods [19]. Advancing technologies for obtaining initial blanks lead to the possibility of abandoning roughing stages of processing and the transition to finishing operations.

Russian structural alloy steel 40X [20] and its foreign counterparts [21] are widely used for the production of various parts and have been well studied. At the same time, changes in the structure of this steel after various types of machining have not been studied sufficiently.

Using transmission electron microscopy (TEM), this work examines the structure of steel 40X after machining by cutting.

EXPERIMENTAL

We investigated steel 40X after recrystallization annealing at a temperature of 600°C for 60 min. Steel samples were subjected to finishing, rough–semifinishing, or rough–semifinishing–finishing turning on

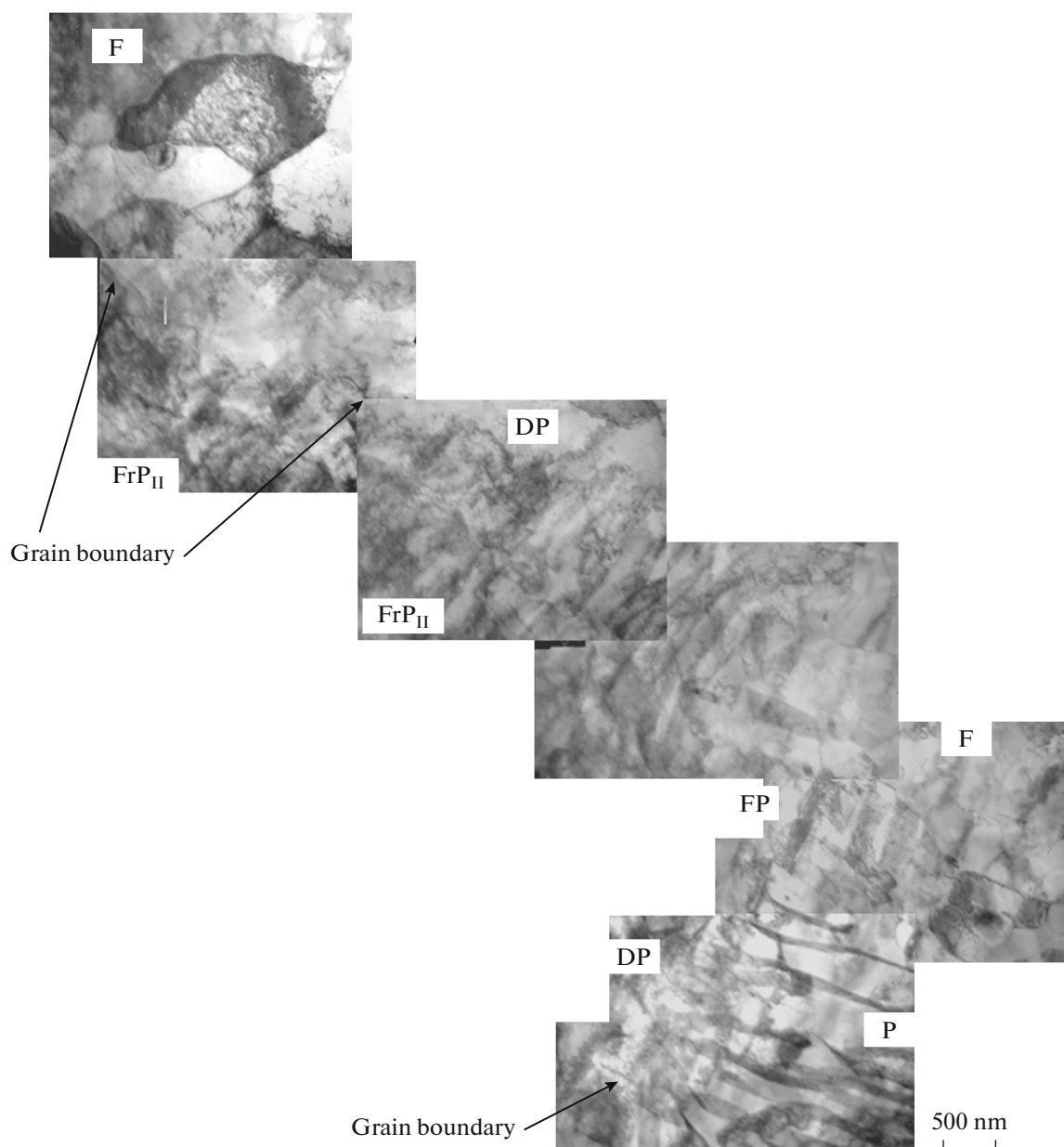


Fig. 1. TEM image of the structure of steel 40X after finishing: P, defect-free lamellar pearlite; DP, destroyed lamellar pearlite; FP, faulty lamellar pearlite; FrP_{II}, secondarily fragmented lamellar pearlite; F, fragmented ferrite.

a 16K20F3 lathe with the NC-210 numerical control system. Machining was carried out using the Korloy cutter with the CNMG120408-VM blade insert.

Finishing turning was carried out for a diameter of 35.5 mm and a cutting depth of 0.25 mm with a feed of 0.1 mm/rev at the rotation speed of 1200 rev⁻¹. Rough–semifinishing turning was carried out by sequential rough turning (cutting depth 1 mm, feed 0.4 mm/rev, rotation speed 650 rev⁻¹) and semifinishing turning (cutting depth 0.5 mm, feed 0.25 mm/rev, rotation speed 900 rev⁻¹) for a diameter of 28.5 mm. Rough–semifinishing–finishing turning was carried

out with a sequential combination of the above modes for a diameter of 28 mm.

The structure of the steel was investigated by transmission electron diffraction microscopy of thin foils using an EM-125 microscope at an accelerating voltage of 125 kV. Samples for microscopy were prepared by electrolytic thinning of foils cut from the sample on an electric spark machine to 0.25–0.30 mm. Phases were identified by microdiffraction patterns according to the methods [22, 23]; quantitative phase analysis was carried out according to the methods [24–26]. The volume fraction of structural components was determined by the planimetric method [24]. The sca-

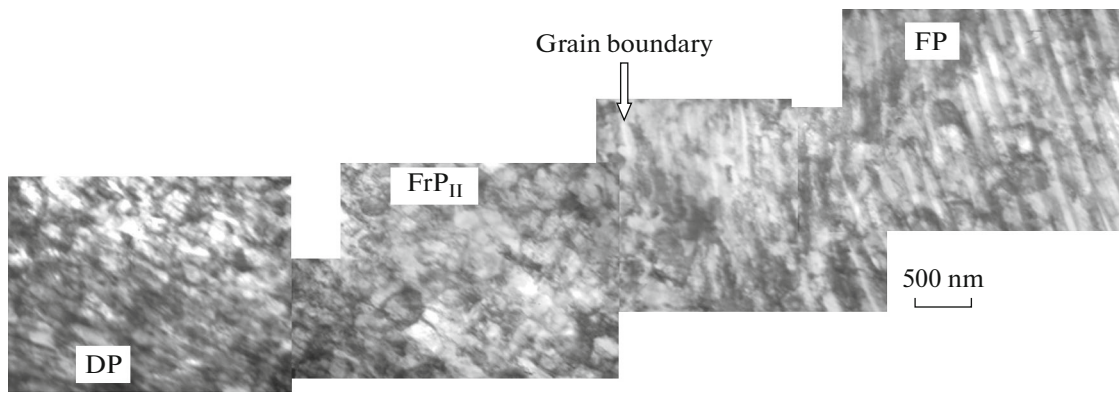


Fig. 2. TEM image of the fine structure of steel 40X after finishing. Lamellar pearlite: DP, destroyed pearlite; FrP_{II}, secondarily fragmented pearlite; FP, faulty pearlite.

lar dislocation density ρ was measured by the secant method [27] and the excess dislocation density $\rho_{\pm} = \rho_{+} - \rho_{-}$ (ρ_{+} and ρ_{-} are the density of positively and negatively charged dislocations, respectively) was measured locally from the misorientation gradient (or from the curvature-torsion of the crystal lattice χ) [28–30]. Internal shear stresses (or forests of dislocations) and long-range stresses were determined [31].

RESULTS AND DISCUSSION

Finishing

Typical TEM images of all morphological structures of lamellar pearlite are shown in Figs. 1–5. All lamellar pearlite formed as a result of finishing can be divided into the following morphological components:

1. Defect-free lamellar pearlite, whose volume fraction was 5% of the total volume of the material.
2. Defect-free lamellar pearlite with curved cementite plates, volume fraction of 5%.
3. Faulty lamellar pearlite, volume fraction of 20%.
4. Destroyed lamellar pearlite, volume fraction of 20%.
5. Primarily fragmented lamellar pearlite, volume fraction of 25%.
6. Secondarily fragmented lamellar pearlite, volume fraction of 5%.

Primarily fragmented lamellar pearlite is a mixture of defect-free and faulty lamellar pearlite with straight and curved cementite plates, with primary fragments formed in the α -phase plates. This combination is due to the closeness of all quantitative parameters in these structures.

Ferrite, the volume fraction of which was 20%, was all fragmented; non-fragmented ferrite was not found.

As can be seen from the figures, grains with different morphological components are present and adjacent to each other in a random manner (Figs. 1 and 2).

Nevertheless, the formation of primary fragments in pearlite is most pronounced near grain boundaries (Figs. 3a, 4, and 5). The formation of secondary fragments in pearlite, apparently, begins in fractured pearlite also near the grain boundary (Figs. 1 and 2). Figure 1 shows that the structure of destroyed pearlite

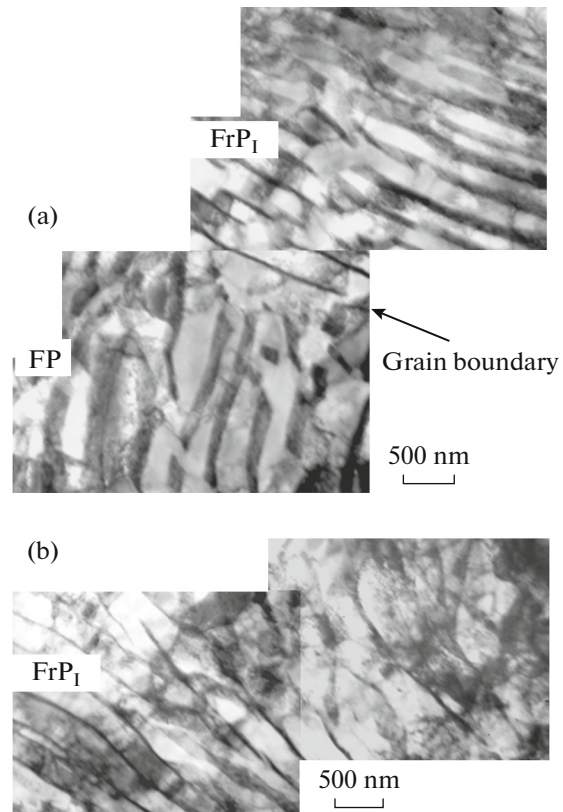


Fig. 3. TEM image of lamellar pearlite of steel 40X after finishing: (a) example of the formation of primary fragments in pearlite near grain boundaries, (b) characteristic structure of primarily fragmented lamellar pearlite. FP, faulty lamellar pearlite; FrP_I, primarily fragmented lamellar pearlite.

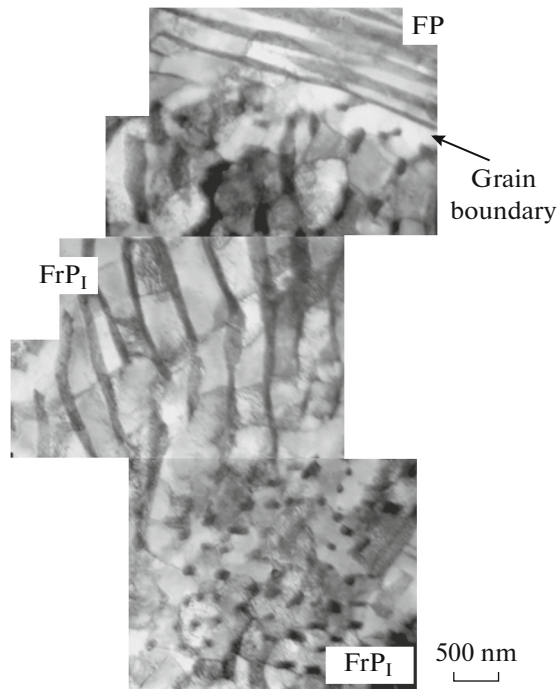


Fig. 4. TEM image of the fine structure of steel 40X after finishing: FP, faulty lamellar pearlite; FrP₁, primarily fragmented lamellar pearlite.

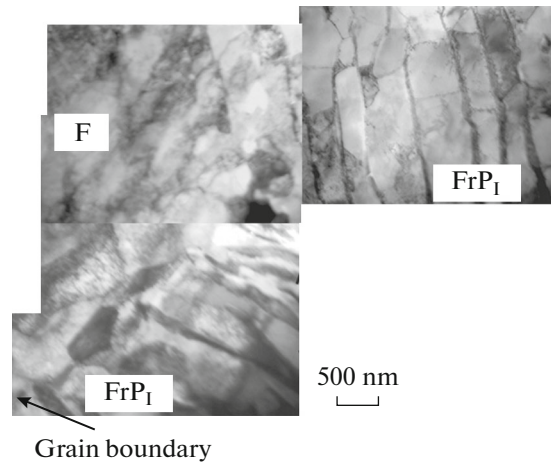


Fig. 5. TEM image of the fine structure of steel 40X after finishing: F, fragmented ferrite; FrP₁, primarily fragmented lamellar pearlite.

contains small fragments, which are most noticeable near the boundary with grains of fragmented ferrite. Figure 2 shows that between grains with faulty and destroyed pearlite there is a section of grains of secondarily fragmented pearlite, but while the boundary with grains of faulty pearlite can be identified quite clearly, no clear boundary between the destroyed and secondarily fragmented pearlite is visible.

Finishing of the sample alters quantitative parameters that characterize the structure; the effect of finish-

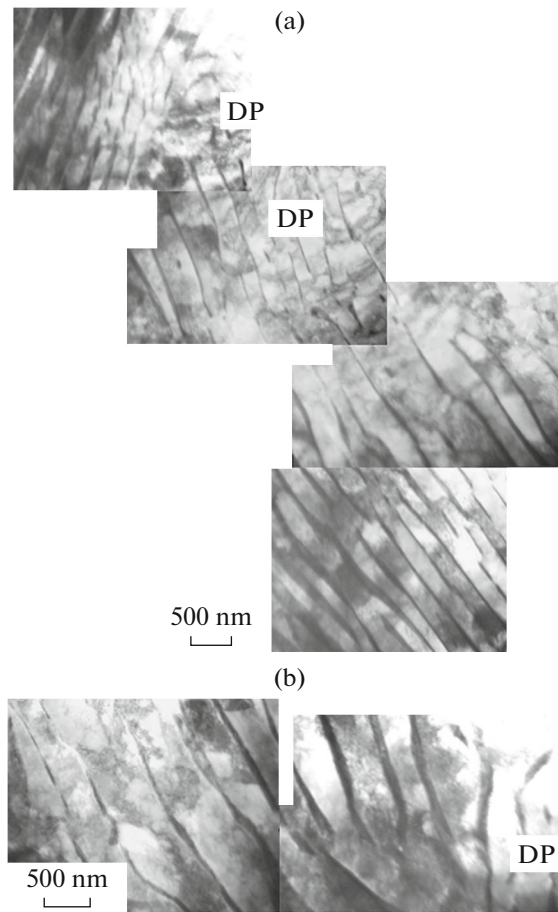


Fig. 6. TEM image of the fine structure of steel 40X after roughing–semifinishing: (a) destroyed areas of pearlite colonies, (b) characteristic morphology of destroyed pearlite colonies. Lamellar defect-free pearlite (areas of destroyed lamellar pearlite DP are marked).

ing on various morphological components of pearlite varied (Table 1).

Curvature-torsion of the α -phase crystal lattice in all morphological components of lamellar pearlite, except for the secondarily fragmented pearlite, is plastic in nature, that is, $\chi = \chi_{pl}$, $\rho > \rho_{\pm}$ and $\sigma_{sh} > \sigma_d$. In the secondarily fragmented pearlite, the curvature-torsion of the α -phase crystal lattice is elastoplastic, that is, $\chi = \chi_{pl} + \chi_{el}$, $\rho < \rho_{\pm}$, and $\sigma_{sh} < \sigma_d$ ($\sigma_d = \sigma_d^{pl} + \sigma_d^{el}$). Here χ is the average curvature-torsion amplitude of the α -phase crystal lattice; χ_{pl} is the curvature-torsion amplitude of the α -phase crystal lattice during plastic deformation; χ_{el} is the curvature-torsion amplitude of the α -phase crystal lattice during elastic deformation; ρ is the scalar dislocation density; ρ_{\pm} is the excess dislocation density; σ_{sh} is the amplitude of internal shear stresses; σ_d is the amplitude of internal local stresses; σ_d^{pl} is the amplitude of internal local stresses during

Table 1. Quantitative parameters of the fine structure of samples after finishing

Morphological component of steel matrix	Scalar dislocation density ρ , 10^{10} cm^{-2}	Excess dislocation density ρ_{\pm} , 10^{10} cm^{-2}	Curvature-torsion of crystal lattice χ , cm^{-1}	Amplitude of internal stresses	
				shear stress σ_{sh} , MPa	local stresses σ_d , MPa
Lamellar pearlite					
Defect-free	2.45	1.88	470	315	275
Defect-free with curved cementite plates	2.94	2.89	705	340	335
Faulty	2.65	2.12	530	325	290
Destroyed	4.05	3.36	840	400	365
Primarily fragmented	3.24	1.78	445	360	265
Secondarily fragmented	3.98	3.98	1000 (905 for pl., 95 for el.)	400	530 (400 for pl., 130 for el.)
In pearlite	3.27	2.47	620 (615 for pl., 5 for el.)	360	315 (305 for pl., 10 for el.)
Ferrite					
Fragmented	3.63	2.92	730	380	340
In ferrite	3.63	2.92	730	380	340
Average in material	3.34	2.56	640 (635 for pl., 5 for el.)	365	320 (310 for pl., 5 for el.)

Table 2. Quantitative parameters of the fine structure of samples after roughing—semifinishing

Morphological component of steel matrix	Scalar dislocation density ρ , 10^{10} cm^{-2}	Excess dislocation density ρ_{\pm} , 10^{10} cm^{-2}	Curvature-torsion of crystal lattice χ , cm^{-1}	Amplitude of internal stresses	
				shear stress σ_{sh} , MPa	local stresses σ_d , MPa
Lamellar pearlite					
Defect-free	3.12	1.84	460	350	270
Defect-free with curved cementite plates	2.40	1.79	470	310	265
Faulty	3.18	3.18	795	355	355
Destroyed	2.80	2.80	700	335	335
In pearlite	3.03	2.35	590	345	305
Ferrite					
Unfragmented	2.57	2.36	590	320	305
Fragmented	2.40	1.08	270	310	235
In ferrite	2.44	1.40	350	310	265
Average in material	2.91	2.16	540	340	290

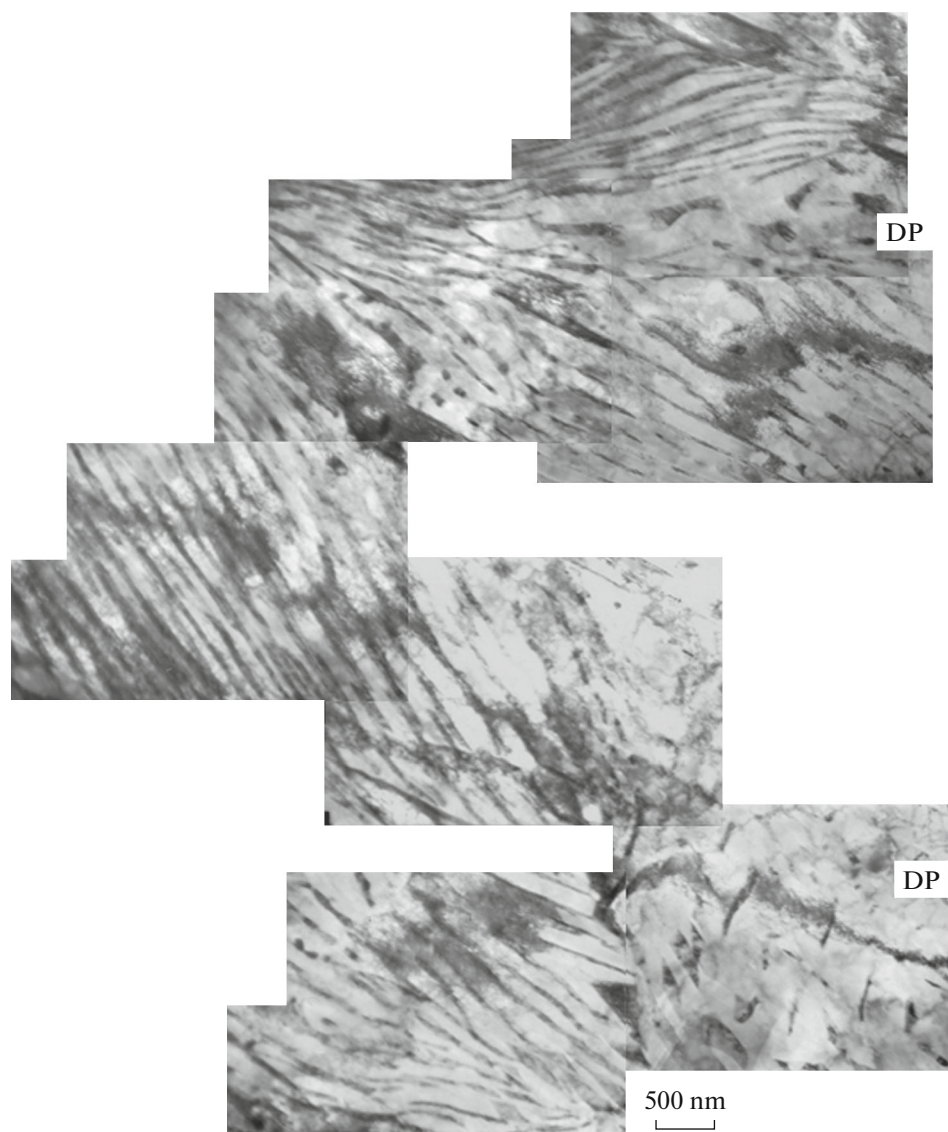


Fig. 7. TEM image of the fine structure of steel 40X after roughing–semifinishing. Lamellar pearlite (DP, destroyed areas of pearlite colonies).

plastic deformation; σ_d^{el} is the amplitude of internal local stresses during elastic deformation.

Since the main part of the steel structure is represented by the pearlite component, the average values of all parameters are determined mainly by their values for the pearlite component. Therefore, in general for the material, values of ρ , ρ_{\pm} , and σ_{sh} were the highest and the value of ρ_d was the lowest. Here, the plastic component σ_d averaged over the material is the highest, while the elastic component is the lowest; therefore, the risk of macrocracking, which can lead to the destruction of the material, is minimal.

Roughing–Semifinishing

This treatment of the sample alters the morphology of the structural components (Figs. 6–10). The main structural components are lamellar defect-free pearlite and destroyed lamellar pearlite (Fig. 6); destroyed areas of pearlite colonies (Fig. 7); defect-free lamellar pearlite with curved cementite plates and faulty lamellar pearlite (Fig. 8); faulty lamellar pearlite and fragmented and non-fragmented ferrite (Fig. 9); and lamellar defect-free pearlite, faulty lamellar pearlite, and fragmented ferrite (Fig. 10).

In defect-free lamellar pearlite (both with straight and curved cementite plates), the dislocation structure is only partially polarized, that is, $\rho > \rho_{\pm}$, while in

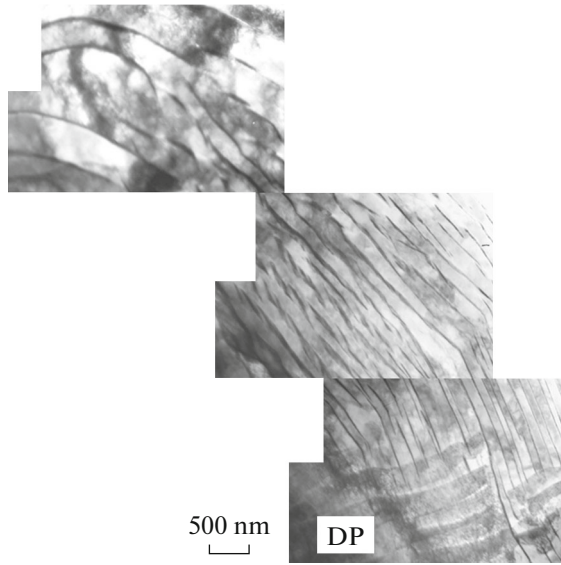


Fig. 8. TEM image of the fine structure of steel 40X after roughing–semifinishing. Defect-free lamellar pearlite with curved cementite plates (FP, area of faulty lamellar pearlite).

faulty and destroyed lamellar pearlite it is completely polarized, that is, $\rho = \rho_{\pm}$.

Ferrite includes both non-fragmented (~5%) and fragmented dislocation substructure (~15%). The cur-

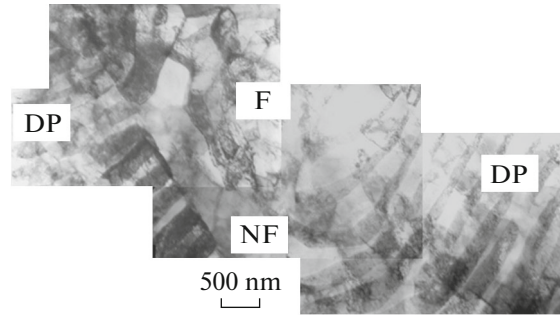


Fig. 9. TEM image of the fine structure of steel 40X after roughing–semifinishing. Faulty lamellar pearlite (FP), fragmented (F), and non-fragmented (NF) ferrite.

vature-torsion of the crystal lattice in non-fragmented ferrite is plastic in nature ($\chi = \chi_{pl}$, $\rho > \rho_{\pm}$), just as in fragmented ferrite (Table 2).

After processing the sample in the roughing–semifinishing mode, pearlite is the main structural component of steel; therefore, the average values of all structural parameters are determined by their values for the pearlite component. Since the treatment significantly reduced such parameters of the structure as χ , ρ_{\pm} , and σ_d , the risk of microcracking in the material is minimized.

Table 3. Quantitative parameters of the fine structure of samples after roughing–semifinishing–finishing

Morphological component of steel matrix	Scalar dislocation density ρ , 10^{10} cm^{-2}	Excess dislocation density ρ_{\pm} , 10^{10} cm^{-2}	Curvature-torsion of crystal lattice χ , cm^{-1}	Amplitude of internal stresses	
				shear stress σ_{sh} , MPa	local stresses σ_d , MPa
Lamellar pearlite					
Defect-free	2.65	1.90	475	325	275
Faulty	2.25	2.18	545	300	295
Destroyed	2.94	2.56	640	340	320
Primarily fragmented	2.35	2.35	625 (585 for pl., 40 for el.)	305	360 (305 for pl., 55 for el.)
Secondarily fragmented	4.12	4.12	1455 (1030 for pl., 425 for el.)	405	985 (405 for pl., 580 for el.)
In pearlite	2.72	2.42	670 (605 for pl., 65 for el.)	330	395 (310 for pl., 85 for el.)
Ferrite					
Fragmented	2.0	1.74	435	280	265
In ferrite	2.0	1.74	435	280	265
Average in material	2.68	2.28	620 (570 for pl., 50 for el.)	320	370 (300 for pl., 70 for el.)

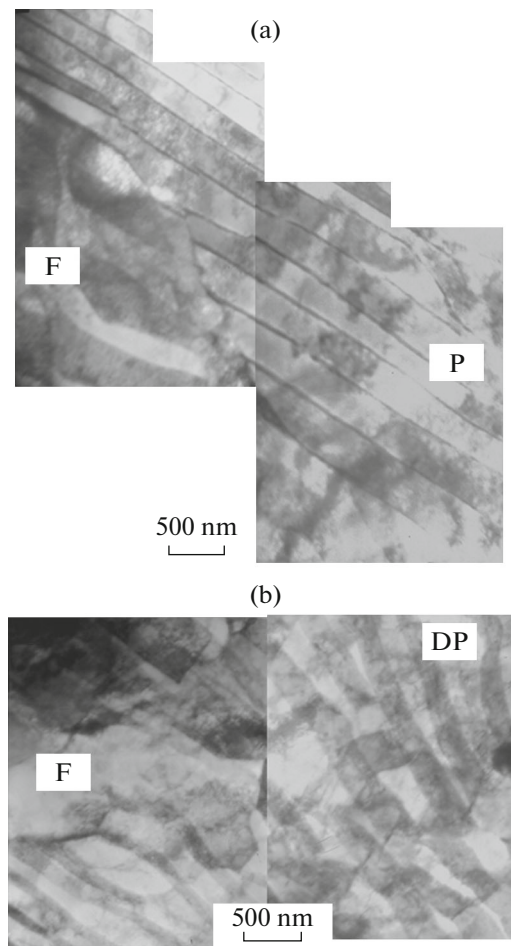


Fig. 10. TEM image of the fine structure of steel 40X after roughing–semifinishing: (a) structure based on defect-free lamellar pearlite and fragmented ferrite, (b) structure based on faulty lamellar pearlite and fragmented ferrite. P, defect-free lamellar pearlite; FP, faulty lamellar pearlite; F, fragmented ferrite.

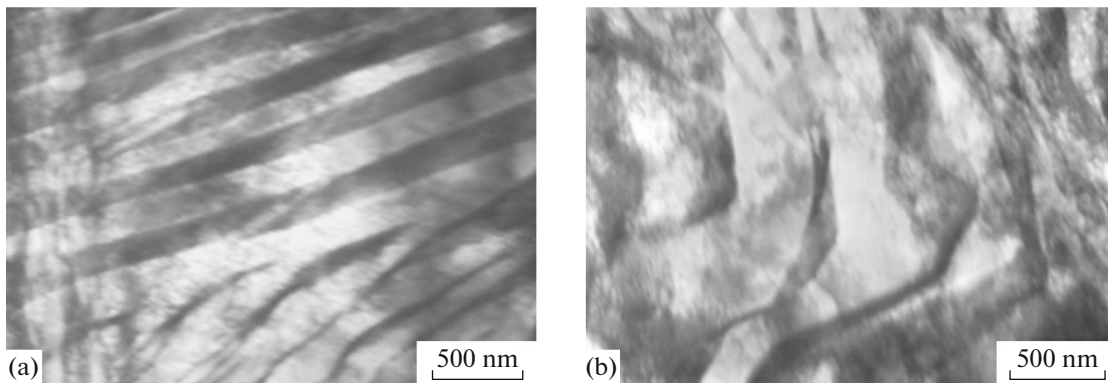


Fig. 11. TEM image of the fine structure of steel 40X after successive roughing–semifinishing–finishing: (a) defect-free lamellar pearlite; (b) defect-free lamellar pearlite with curved cementite plates.

Roughing–Semifinishing–Finishing

Micrographs of the steel structure after roughing–semifinishing–finishing are shown in Figs. 11–14. The main structural components are defect-free

lamellar pearlite and defect-free lamellar pearlite with curved cementite plates (Fig. 11), primarily fragmented lamellar pearlite (Fig. 12), primarily and secondarily fragmented lamellar pearlite (Fig. 13), and fragmented ferrite, secondarily fragmented lamellar

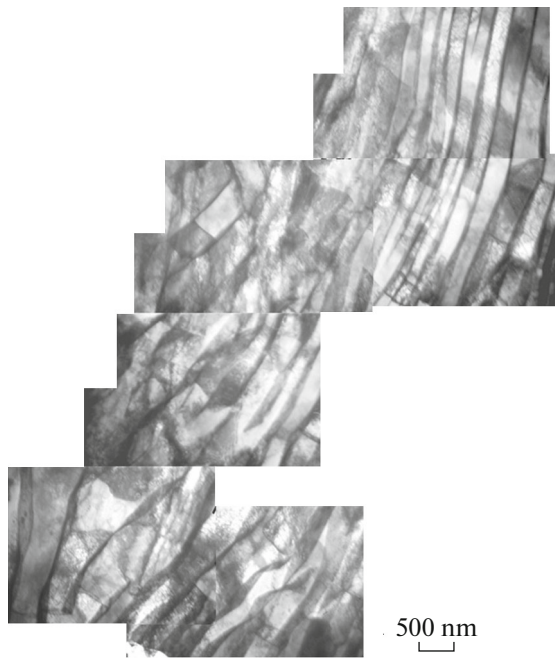


Fig. 12. TEM image of the fine structure of steel 40X after successive roughing–semifinishing–finishing. Primarily fragmented lamellar pearlite.

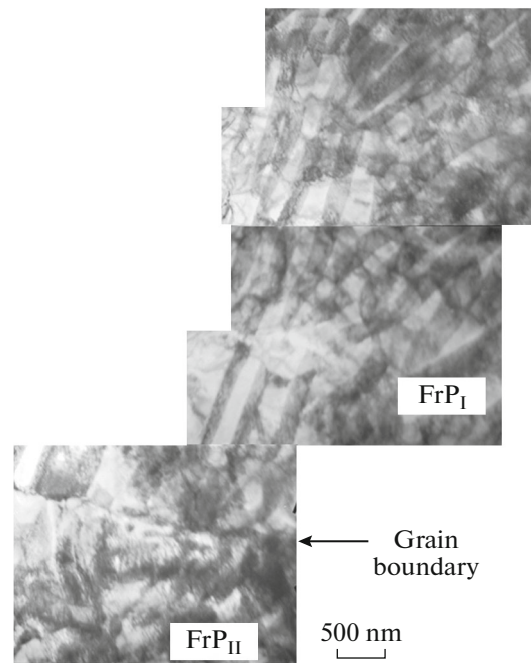
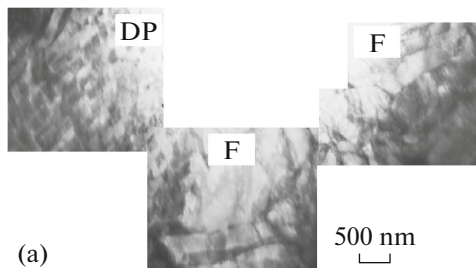
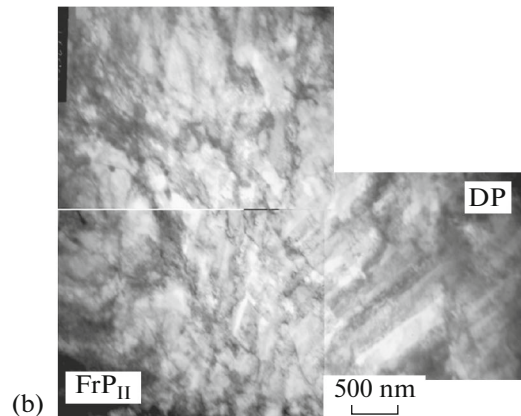


Fig. 13. TEM image of the fine structure of steel 40X after successive roughing–semifinishing–finishing. Primary (FrP_I) and secondary (FrP_{II}) fragmented lamellar pearlite.



(a)



(b)

Fig. 14. TEM image of the fine structure of steel 40X after successive roughing–semifinishing–finishing: (a) structure based on destroyed lamellar pearlite with preserved orientation of pearlite plates and fragmented ferrite, (b) structure based on destroyed lamellar pearlite with preserved directionality of pearlite plates and secondarily fragmented lamellar pearlite. F, fragmented ferrite; FrP_{II}, secondarily fragmented lamellar pearlite; DP, destroyed lamellar pearlite with preserved orientation of pearlite plates.

pearlite, and destroyed lamellar pearlite with the preserved orientation of pearlite plates (Fig. 14). Table 3 shows values of the parameters characterizing the structure of all the presented morphological components of the steel (scalar dislocation density; width of bending extinction contours, which were used to determine the amplitude of curvature-torsion of the α -phase crystal lattice; the excess dislocation density; and the amplitude of internal stresses in different areas of the material).

In both the morphological components of fragmented pearlite, the plastic component of curvature-torsion of the α -phase crystal lattice exceeds the elastic one: in primarily fragmented pearlite, the χ_{pl} value is higher than χ_{el} by ~ 15 times; in fragmented pearlite, it is higher by 2.5 times. The plastic component of the amplitude of long-range stresses is greater than the elastic component: in the primary fragments of pearlite by 5.5 times, while in the secondary fragments, on the contrary, the elastic component is almost 1.5 times larger than the plastic one.

CONCLUSIONS

1. Regardless of the machining mode applied to steel 40X, the main morphological components of the structure are lamellar pearlite (defect-free, faulty, destroyed, and fragmented) and ferrite (fragmented and non-fragmented). The volume fractions of morphological components depend on the machining mode.

2. Finishing carried out without preliminary stages leads to the formation of a faulty substructure in 95% of the material volume (20% ferrite + 75% lamellar pearlite). After roughing—semifinishing, a faulty substructure is formed in 50% of the volume (15% ferrite + 35% lamellar pearlite). Sequential roughing—semifinishing—finishing leads to the formation of a faulty substructure in 75% of the material volume (20% ferrite + 55% lamellar pearlite).

3. Despite the high fragmentation of the structure, the probability of microcracking during finishing is minimal. Roughing—semifinishing—finishing leads to the formation of a higher plastic component of the amplitude of long-range stresses, and the areas of nucleation of secondary fragments may give rise to microcracks.

FUNDING

This study was carried out with the financial support of the Grant of the President of the Russian Federation for State Support of Young Russian Scientists—Doctors of Science MD-486.2020.8, as well as with the financial support of the Russian Foundation for Basic Research within the framework of scientific project no. 20-08-00044.

CONFLICT OF INTEREST

The authors declare that they have no conflicts of interest.

REFERENCES

- Jha, N.K., Singh, T., Dvivedi, A., and Rajesha, S., Experimental investigations into triplex hybrid process of GA-RDECDM during subtractive processing of MMC's, *Mater. Manuf. Processes*, 2019, vol. 34, pp. 243–255.
- Genga, R.M., Rokebrand, P., Cornish, L.A., Zeman, P., Brajer, J., Woydt, M.F., van Vuuren, A.J., and Polese, C., Roughing, semi-finishing and finishing of laser surface modified nickel bonded NbC and WC inserts for grey cast iron (GCI) face-milling, *Int. J. Refract. Met. Hard Mater.*, 2020, vol. 86, art. ID 105128.
- Ringgaard, K., Mohammadi, Y., Merrild, C., Balling, O., and Ahmadi, K., Optimization of material removal rate in milling of thin-walled structures using penalty cost function, *Int. J. Mach. Tools Manuf.*, 2019, vol. 145, art. ID 103430.
- Yang, Y., Zhang, W.H., Ma, Y.C., Wan, M., and Dang, X.B., An efficient decomposition-condensation method for chatter prediction in milling large-scale

thin-walled structures, *Mech. Syst. Signal Process.*, 2019, vol. 121, pp. 58–76.

- Guo, M., Jiang, X., Ye, Y., Ding, Z., and Zhang, Z., Investigation of redistribution mechanism of residual stress during multi-process milling of thin-walled parts, *Int. J. Adv. Manuf. Technol.*, 2019, vol. 103, pp. 1459–1466.
- Mittal, S., Dutta, M.K., and Issac, A., Non-destructive image processing based system for assessment of rice quality and defects for classification according to inferred commercial value, *Measurement*, 2019, vol. 148, art. ID 106969.
- Zhai, J., Wang, H., Chen, P., Hu, Y., and Sun, W., Recycling of iron and titanium resources from early tailings: From fundamental work to industrial application, *Chemosphere*, 2020, vol. 242, art. ID 125178.
- Hojati, F., Daneshi, A., Soltani, B., Azarhoushang, B., and Biermann, D., Study on machinability of additively manufactured and conventional titanium alloys in micro-milling process, *Precis. Eng.*, 2020, vol. 62, pp. 1–9.
- Liu, J., Anderson, K.L., and Sridhar, N., Direct simulation of polymer fused deposition modeling (FDM)—an implementation of the multi-phase viscoelastic solver in open foam, *Int. J. Comput. Methods*, 2020, vol. 17, art. ID 1844002.
- Nong, X.D., Zhou, X.L., Li, J.H., Wang, Y.D., Zhao, Y.F., and Brochu, M., Selective laser melting and heat treatment of precipitation hardening stainless steel with a refined microstructure and excellent mechanical properties, *Scripta Mater.*, 2020, vol. 178, pp. 7–12.
- Zhang, Z., Yao, X.X., and Ge, P., Phase-field-model-based analysis of the effects of powder particle on porosities and densities in selective laser sintering additive manufacturing, *Int. J. Mech. Sci.*, 2020, vol. 166, art. ID 105230.
- Manière, C., Kerbart, G., Harnois, C., and Marinel, S., Modeling sintering anisotropy in ceramic stereolithography of silica, *Acta Mater.*, 2020, vol. 182, pp. 163–171.
- Mele, M., Campana, G., and Monti, G.L., Modelling of the capillarity effect in multi jet fusion technology, *Addit. Manuf.*, 2019, vol. 19, art. ID 100879.
- Park, J.Y., Kim, H.Y., Kim, J.H., Kim, J.-H., and Kim, W.C., Comparison of prosthetic models produced by traditional and additive manufacturing methods, *J. Adv. Prosthodontics*, 2015, vol. 7, pp. 294–302.
- Rangarajan, S., Sunitha, K., and Annamahesh, A., Analysis of part built orientation of the polyjet 3D printed polymer component, *Int. J. Innovative Technol. Explor. Eng.*, 2019, vol. 8, pp. 3355–3358.
- Altintas, Y., Torun, I., Yazici, A.F., Beskacak, E., Erdem, T., Serdar Onses, M., and Mutlugun, E., Multi-plexed patterning of cesium lead halide perovskite nanocrystals by additive jet printing for efficient white light generation, *Chem. Eng. J.*, 2020, vol. 380, art. ID 122493.
- Romanov, D.A., Moskovskii, S.V., Martusevich, E.A., Gayevoy, E.A., and Gromov, V.E., Structural-phase state of the system “CdO-Ag coating/copper substrate” formed by electroexplosive method, *Metallurgiya*, 2018, vol. 57, pp. 299–302.
- Romanov, D.A., Moskovskii, S.V., Sosnin, K.V., Gromov, V.E., and Bataev, V.A., Structure and electrical

- erosion resistance of an electro-explosive coating of the CuO–Ag system, *Mater. Res. Express*, 2019, vol. 6, no. 5, art. ID 055042.
19. Fernando, S., Weir, S., Reinhardt, D., and Hannouch, A., Towards a multi-criteria framework for stereotomy – Workflows for subtractive fabrication in complex geometries, *J. Comput. Des. Eng.*, 2019, vol. 6, pp. 468–478.
 20. Sandomirskii, S.G., Monitoring the physicomachanical properties of 40X steel on the basis of the limiting magnetic hysteresis loop, *Steel Transl.*, 2018, vol. 48, pp. 330–334.
 21. Korotkov, V.A., Influence of plasma quenching on the wear resistance of 45 and 40X steel, *Russ. Eng. Res.*, 2016, vol. 36, pp. 916–919.
 22. Utevskaia, L.M., *Difraktsionnaya elektronnaia mikroskopiia v metallovedenii* (Diffraction Electron Microscopy in Metals Science), Moscow: Metallurgiya, 1973.
 23. Andrews, W., Dyson, D.J., and Keown, S.R., *Interpretation of Electron Diffraction Patterns*, Boston: Springer, 1967.
 24. Saltykov, S.A., *Stereometricheskaya metallografiia* (Stereometric Metallography), Moscow: Metallurgiya, 1970.
 25. Chernyavskiy, K.S., *Stereologiya v metallovedenii* (Stereology in Metals Science), Moscow: Metallurgiya, 1977.
 26. Bogachev, I.N., Vainshtein, A.A., and Volkov, S.D., *Vvedenie v statisticheskoe metallovedenie* (An Introduction into Statistical Metals Science), Moscow: Metallurgiya, 1972.
 27. Hirsch, P.B., Howie, A., Nicholson, R.B., Pashley, D.W., and Whelan, M.J., *Electron Microscopy of Thin Crystals*, London: Butterworths, 1965.
 28. Koneva, N.A. and Kozlov, E.V., Nature of substructural hardening, *Sov. Phys. J.*, 1983, vol. 25, pp. 681–691.
 29. Koneva, N.A. and Kozlov, E.V., Physical nature of stages of plastic strain, in *Strukturnye urovni plasticheskoi deformatsii i razrusheniia* (Structural Levels of Plastic Strain and Failure), Novosibirsk: Nauka, 1990, pp. 123–186.
 30. Koneva, N.A., Kozlov, E.V., Trishkina, L.I., and Ly-chagin, D.V., Long-range stress fields, bend-twist of crystal lattice, and stages of plastic deformation. Methods of measurement and results, in *Novye metody v fizike i mekhanike deformiruемого tverdogo tela* (New Methods in the Physics and Mechanics of Solids), Panin, V.E., Ed., Tomsk: Tomsk State Univ., 1990, ch. 1, pp. 83–93.
 31. Koneva, N.A. and Kozlov, E.V., Regularities of substructural hardening, *Sov. Phys. J.*, 1991, vol. 34, pp. 224–236.

Translated by K. Lazarev